PAPER

Check for updates

Defects or no defects? Or how to design 20–25 nm spherical iron oxide nanoparticles to harness both magnetic hyperthermia and photothermia†

Barbara Freis,[a,b] Céline Kiefer,[a] Maria de los Angeles Ramirez,[a] Sébastien Harlepp,[c,d,e] Damien Mertz, [ID][a] Benoit Pichon,[a] Cristian Iacovita, [ID] *[f] Sophie Laurent [ID][b] and Sylvie Begin [ID] *[a]

Designing iron oxide nanoparticles (IONPs) to effectively combine magnetic hyperthermia (MH) and photothermia (PTT) in one IONP formulation presents a significant challenge to ensure a multimodal therapy allowing the adaptation of the treatment to each patient. Recent research has highlighted the influence of factors such as the size, shape, and amount of defects on both therapeutic approaches. In this study, 20–25 nm spherical IONPs with a spinel composition were synthesized by adapting the protocol of the thermal decomposition method to control the amount of defects. By tuning different synthesis parameters such as the precursor nature, the introduction of a well-known oxidizing agent, dibenzylether (DBE), in the reaction medium, the heating rate and duration and the introduction of a nucleation step, we thus established two different synthesis protocols, one involving the use of a small amount of DBE leading to IONPs with only a few defects and another that took an optimized route to oxidize the wüstite nuclei during the IONP growth and led to IONPs exhibiting more structural and oxygen defects. IONPs exhibiting fewer defects showed enhanced MH and PTT heating values even when immobilized in a matrix, despite a decrease in MH heating values showing that they release mainly heat through the Brownian mechanism. These MH measurements have also confirmed that defects play a key role in enhancing Néel relaxation. PTT measurements demonstrated higher heating values with IONPs with fewer defects and a correlation between Urbach energy and SAR values suggesting an impact of vacancy defects on PTT performances. Therefore, IONPs exhibiting fewer defects under our synthesis conditions appear as suitable IONPs to combine both MH and PTT treatments with high performances. These findings pave the way for promising applications in combined therapies for cancer treatment.

[a]Université de Strasbourg, CNRS, Institut de Physique et Chimie des Matériaux, UMR CNRS-UdS 7504, 23 Rue du Loess, BP 43, 67034 Strasbourg, France. E-mail: sylvie.begin@unistra.fr
[b]Laboratoire de NMR et d'imagerie moléculaire, Université de Mons, Avenue Maistriau 19, 7000 Mons, Belgium
[c]Institut de Cancérologie Strasbourg Europe, 67000 Strasbourg, France
[d]Equipe Labellisée Ligue Contre le Cancer, France
[e]Strasbourg Drug Discovery and Development Institute (IMS), 67000 Strasbourg, France
[f]Department of Pharmaceutical Physics-Biophysics, Faculty of Pharmacy, Iuliu Hatieganu University of Medicine and Pharmacy, 6 Pasteur St., 400349 Cluj-Napoca, Romania. E-mail: cristian.iacovita@umfcluj.ro
†Electronic supplementary information (ESI) available. See DOI: https://doi.org/10.1039/d4nr01397b

I. Introduction

Spherical spinel iron oxide nanoparticles (IONPs) with sizes in the range 20–25 nm are promising for magnetic hyperthermia (MH) when the size of IONPs has less impact on photothermia (PTT) performance.[1–6] In MH, IONPs, upon exposure to an alternating magnetic field (AMF), generate localized heat effective against cancer cells, which are more sensitive to temperature increases than healthy cells.[7–10] However, MH's efficacy is hindered by limited heating power, often requiring high local doses of IONPs.[2,7,11–13] Enhancing the performance of IONPs is crucial and is generally achieved through increasing saturation magnetization (M_s) and effective anisotropy.[2,8,14–16] Larger-sized IONPs exhibit higher M_s improving MH efficiency.[2,11,16,17] Despite their promise, IONPs of 20–25 nm size were shown to primarily release heat through Brownian relaxation rather than Néel relaxation, which diminishes their

efficacy when located within cells or tissues.[9,18–22] Factors such as NP aggregation and immobilization upon interaction with cells contribute to this decrease, affecting their MH efficiency.[7,9,18,19,22,23] Additionally, defects within IONPs have been reported to improve MH performance by favoring Néel relaxation in cellular environments.[23–25]

Recent studies have shown that IONPs are also effective for photothermal therapy (PTT) by converting absorbed light into localized heating when exposed to near-infrared laser irradiation. This process would be facilitated by d–d electron transitions, moving electrons from conduction to valence bands.[26] Since Yu et al.'s initial report in 2011,[27] IONPs have consistently proved to be efficient in generating heat under laser irradiation.[4,5,26,28,29] Factors influencing heat release remain somewhat unclear. While some studies suggest that the IONP shape affects heating,[4,5] others argue that the crystallographic structure, rather than size or shape, is the primary determinant of PTT effectiveness.[6,26,29,30] Bertuit et al.[30] examined iron oxide nanoflowers with varying levels of defects and found that excessive defects (oxygen vacancies) led to diminished PTT performance. They attributed this behavior to the trapping of electrons by oxygen vacancies, hindering electron transfer responsible for heat generation.

The recent use of IONPs as PTT nano-heaters offers a novel dual treatment method by combining MH and PTT. This approach benefits from a reduced IONP dose and enhanced MH through laser irradiation. 20–25 nm iron oxide-based nanospheres hold potential for merging MRI and hyperthermia therapy, including PTT and MH. However, the presence of defects appears to have an antagonistic effect on both MH and PTT. Two main types of defects have been noticed: oxygen vacancy defects as reported by Bertuit et al.[30] and structural defects such as dislocation and/or antiphase boundaries. The presence of a wüstite core is often observed using the thermal decomposition method (especially when targeting IONPs with a mean size higher than 15 nm), as the nuclei exhibit a wüstite composition.[31,32] Structural defects have been reported to form during the oxidation of $Fe_{1-x}O$ in the magnetite phase.[7,11,33] Indeed, our previous studies on core–shell $Fe_{1-x}O@Fe_{3-x}O_4$ nanocubes[33,34] and the work of Wetterskog et al.[35] have shown that the post-oxidation of $Fe_{1-x}O$ induced the formation of lattice dislocations and/or antiphase boundaries in NPs. Dibenzyl ether has been demonstrated to be an effective oxidizing agent[7,36,37] either used as solvent or added to the reaction medium. However, to obtain IONPs with a mean size higher than 15 nm, as the core is wüstite, there is competition between the growth and oxidation kinetics, which may be tuned by adjusting synthesis conditions.[31]

This work investigates the influence of synthesis parameters and dibenzyl–ether (DBE) quantity on the characteristics of iron oxide nanoparticles (IONPs), focusing on size, composition, and defect levels. The challenge lies in consistently producing, using the thermal decomposition method, spherical IONPs in the range of 20–25 nm to be able to combine both MH and PTT therapies. Our aim is to adapt this synthesis method by tuning synthesis parameters to obtain IONPs with precise control over composition and defect levels. Defects, stemming from oxidation processes, including oxygen vacancies and structural irregularities, are crucial in determining the efficiency of MH and PTT combination. We analyze the impact of various parameters like the precursor nature, reaction temperature, heating rate, and DBE amount on the characteristics of IONPs. Both homemade and commercial iron stearates, along with different DBE levels, influence the size, composition, and defects of IONPs. Additionally, an oxidation treatment on core–shell IONPs yields promising results for magnetic and MH properties. Our goal is to design IONPs capable of effectively combining PTT and MH treatments, assessed separately through MH and PTT performance evaluations.

II. Materials and methods

II.1. Materials

Iron stearate ($FeSt_3$) was either homemade[12,38,39] from sodium stearate (purity: 98.8%) purchased from TCI and ferric chloride (purity 99%) purchased from Sigma-Aldrich, or directly purchased from TCI (purity minimum 60% of stearic acid and 5.8 to 7% of iron, and maximum 10% of free acid). Acetone (purity 99.8%), chloroform (purity 99%), hexane (purity 99%) and THF (purity 99.5%) were purchased from Carlo Erba. Dioctyl ether (OE) (purity 99%) was purchased from Sigma-Aldrich. Oleic acid (OA) (purity 99%) was purchased from Alfa Aesar. Dibenzylether (DBE) (purity 98%) and squalane (purity 99%) were purchased from Acros Organics. The dendron D1-2P was provided by SuperBranche.

II.2. Precursor synthesis

Iron stearate(III) was synthesized by precipitating sodium stearate (NaSt) and ferric chloride ($FeCl_3$) salts in water.[12] Sodium stearate (9.8 g, 32 mmol) was dissolved in distilled water (80 mL) in a round-bottomed flask, heated to reflux, and stirred until fully dissolved. Separately, ferric chloride (2.88 g, 10.6 mmol) was dissolved in water (40 mL) and added to the sodium stearate solution under vigorous stirring, resulting in immediate formation of a light orange precipitate. After 15 minutes of stirring at this temperature, the solution was cooled down to room temperature. The precipitate was washed once by centrifugation (14 000 rpm, 10 min), and then filtered with a Büchner funnel and oven-dried at 65 °C for 24 hours, yielding approximately 9 g of the precursor. One batch of the precursor was sufficient for four 20 nm IONP syntheses.

II.3. 20 nm spherical IONP synthesis

For 20 nm spherical IONP synthesis, several protocols were tested and are discussed in this work. Only the two main protocols for the synthesis of reproducible 20 nm spherical NPs are described hereafter. All the syntheses were performed in air.

Protocol P20_1. 2.2 mmol of $FeSt_3$ (1.99 g) and 4.4 mmol of OA (1.24 g) were mixed with squalane (15.8 g, 19.5 mL) and

2.6 mmol of dibenzylether (0.53 g, 0.5 mL) in a two-neck round-bottom-flask of 100 mL. The mixture was first heated to 120 °C (heating device temperature: 130 °C) for 60 min to dissolve the reagents in squalane. After this step, the condenser was connected to the flask and the mixture was heated up to 330 °C (heating device temperature: 360 °C) with a 5 °C min^{-1} ramp. The mixture was refluxed at 330 °C for 120 min. The obtained black NP suspension was cooled down to 100 °C to proceed to the washing step.

Protocol P20_2. 2.0 mmol of FeSt$_3$ (1.85 g) and 6.7 mmol of OA (1.90 g) were mixed with squalane (15.8 g, 19.5 mL) and 2.6 mmol of dibenzylether (0.53 g, 0.5 mL) in a two-neck round-bottom-flask of 100 mL. The mixture was first heated to 120 °C (heating device temperature: 130 °C) for 60 min to dissolve the reagents in squalane. After this step, the condenser was connected to the flask and the mixture was heated up to 330 °C (heating device temperature: 360 °C) with a 5 °C min^{-1} ramp. The mixture was refluxed at 330 °C for 60 min. The obtained black NP suspension was cooled down to 100 °C to proceed to the washing step.

Protocol P20_3_no_DBE. 2.0 mmol of FeSt$_3$ (1.85 g) and 6.7 mmol of OA (1.90 g) were mixed with squalane (16.2 g, 20 mL) in a two-neck round-bottom-flask of 100 mL. The mixture was first heated to 120 °C (heating device temperature: 130 °C) for 60 min to dissolve the reagents in squalane. After this step, the condenser was connected to the flask and the mixture was heated up to 280 °C (heating device temperature: 310 °C) with a 5 °C min^{-1} ramp. The mixture was refluxed at 280 °C for 30 min. After this step, the condenser was connected to the flask and the mixture was heated up to 330 °C (heating device temperature: 360 °C) with a 1 °C min^{-1} ramp. The mixture was refluxed at 330 °C for 60 min. The obtained black NP suspension was cooled down to 100 °C to proceed to the washing step.

Washing step. The same washing step was performed on NPs synthesized from either protocol P20_DBE or P20_NO_DBE. 10 mL of chloroform was added to the IONP suspension at a temperature around 100 °C. Then, this suspension was introduced in a flask containing 400 mL of acetone. This mixture was put on a magnet to collect the IONPs and discard the supernatant. The collected IONPs were redispersed in 50 mL of chloroform. 400 mL of acetone was added again to proceed to a washing step: the mixture was heated at 60 °C for 45 min under mechanical stirring. In the end, the IONPs were collected with a magnet and the supernatant was discarded. Finally, the IONPs were resuspended in 40 mL of THF for their storage or further utilization.

II.4. Oxidation process of core–shell IONPs

5 ml of a suspension of core–shell IONPs (Fe$_{1-y}$O@Fe$_{3-x}$O$_4$) suspended in THF were mixed with 5 mL of dioctylether and 0.5 g of OA in a two-neck round-bottom-flask of 100 mL. The mixture was heated to 120 °C (heating device temperature: 130 °C) for 30 min and the IONPs were resuspended in 10 mL of THF for their storage or further utilization.

II.5. Dendronization step

After synthesis, the IONPs are coated with OA and suspended in THF. Subsequently, a ligand exchange is performed in THF to replace the OA with dendron molecules. The dendron is composed of a bi-phosphonate anchoring group to ensure a robust link to the NP surface, and three PEG chains for biocompatibility and stability in water (Fig. S1†). The central PEG chain is longer and terminated with a carboxylate function, enabling the attachment of additional molecules such as dyes or targeting ligands.[44] The ligand exchange between OA and the dendron (D1-2P) (Fig. S1†) was performed in THF. Briefly, 5 mL of IONPs@OA at 1 mg Fe mL^{-1} was stirred for 48 hours with 10 mg of dendron. To maximize the ligand exchange and remove most of the oleic acid molecules, the suspension was then purified by ultrafiltration. After that, 5 mg of dendron was added to the mixture for another 48 hours of stirring. The suspension was mixed with hexane (volume ratio 1/3 : 2/3) to precipitate the DNPs. The suspension was centrifuged at 8000 rpm for 5 min and the supernatant was discarded. Finally, the DNPs were collected and dispersed in deionized water. The water suspension was purified by ultrafiltration 3 times.

II.6. Characterization techniques

Fourier-transform infrared (FTIR) spectroscopy. Standard infrared spectra were recorded between 4000 cm^{-1} and 400 cm^{-1} with a FTIR spectrometer, Spectrum 100 from PerkinElmer, on both iron precursors and IONP samples. The samples were ground and diluted in a non-absorbent KBr matrix before their analysis. The iron precursor powders were characterized by attenuated total reflectance (ATR) FTIR spectroscopy to examine their main bands corresponding to alkyl chains (peaks between 2800 cm^{-1} and 3000 cm^{-1}), "iron" in iron stearate (a band at 720 cm^{-1}) and carboxylate-based groups (between 1700 cm^{-1} and 1300 cm^{-1}). The FITR spectra of IONP samples allowed us to assess the presence of the characteristic band corresponding to the spinel structure between 800 cm^{-1} and 400 cm^{-1}, the presence of the characteristic bands of oleic acid (alkyl bands between 3000 cm^{-1} and 2800 cm^{-1}) and more importantly, the disappearance of the characteristic band of the iron precursor at 720 cm^{-1}.

Thermogravimetric analysis (TGA). To investigate the thermal decomposition of the different batches of FeSt$_3$, TGA coupled with differential thermal analysis (DTA) was performed on dried powder samples from 20 to 600 °C at 5 °C min^{-1} in air by using an SDJ Q600 apparatus. Differential thermogravimetric measurements were obtained after a first-order differentiation calculation using OriginLab Software.

Transmission electron microscopy (TEM). To have access to their size and morphology, the IONPs were characterized by TEM with a JEOL 2013 microscope operating at 200 kV (point resolution 0.18 nm). The size distribution of NPs was estimated from the size measurements of more than 300 nanoparticles using ImageJ software. High-resolution (HR-TEM) images were also recorded to analyze crystallographic plans and to check the amount of structural defects.

X-ray diffraction (XRD). The XRD patterns allow identifying the crystalline phases of as synthesized IONPs. It is a quick way to identify core–shell nanoparticles with the characteristic peaks of the wüstite phase. However, it is more complicated to differentiate maghemite from magnetite as they exhibit similar XRD patterns. Refinement of the XRD patterns is thus necessary to compare the lattice parameter of the IONPs to those of magnetite and maghemite phases and to check if the composition is closer to that of maghemite or magnetite. Briefly, IONPs suspended in organic solvent (chloroform or THF) were dried on XRD silicium sample holders. The XRD patterns were collected at room temperature with a Bruker D8 Discover diffractometer in Bragg Brentano geometry equipped with a monochromatic copper radiation source ($K\alpha1$ = 0.154056 nm) and an energy-resolved LYNXEYE XE-T detector in the 25–65° (2θ) range with a scan step of 0.03°. High-purity silicon powder (a = 0.543082 nm) was used as an internal standard. The diffraction patterns were refined by LeBail's method using the FullProf software. The background, modeled as a linear function based on 20 experimental points, was refined, as well as the zero shift. The peaks were modeled with the modified Thompson–Cox–Hastings (TCH) pseudo-Voigt profile function.

X-ray photoelectron spectroscopy (XPS). To assess the chemical bonds, present on the IONP surface, XPS was performed on various suspensions. The X-ray photoelectron spectroscopy (XPS) measurements were performed on a Thermo VG spectrometer, using Al $K\alpha$ radiation ($h\nu$ = 1486.6 eV). Survey and high-resolution spectra were recorded in constant pass energy mode (100 and 20 eV, respectively). The binding energy scale was corrected for electrostatic charging using the C 1s peak of adventitious carbon at 284.6 eV as an internal reference.

Ultraviolet–visible–near-infrared spectroscopy (UV-vis-NIR). To determine defect levels in various IONP batches, ultraviolet–visible–near-infrared (UV-vis-NIR) spectroscopy was performed to determine the band gap energy E_g of the samples and their Urbach energy E_u (see the ESI†). UV-vis-NIR spectra of IONP suspension at a concentration of 0.05 mg Fe mL^{-1} in chloroform were recorded between 1100 nm and 250 nm at room temperature in a 1 cm^3 quartz cuvette using a Lambda 950 UV-vis spectrometer from PerkinElmer.

Dynamic light scattering (DLS) and zeta potential. DLS measurements were performed on a Malvern analyser (ZetaSizer Nano) to assess the colloidal stability of the IONP suspension in organic solvent or of DNPs in water and to determine their mean hydrodynamic diameter (D_h). The zeta potential was recorded using the same equipment. The coupling of the TL was confirmed by an increase of D_h and a change in zeta potential values.

Magnetic measurements. Magnetic measurements were conducted using a superconducting Quantum Interference Device (SQUID) magnetometer (MPMS SQUID VSM). To prepare the samples, 50 μL of a known concentration suspension of IONPs in chloroform or THF were introduced in a special capsule, which served as the sample holder for the SQUID apparatus. The solvent was let to evaporate. This process was repeated until we achieved a uniform layer of dried IONPs covering the bottom of the capsule. We then proceeded to record zero-field-cooled (ZFC) and field-cooled (FC) curves as follows: the sample within the SQUID apparatus was initially cooled to 5 K with no applied magnetic field following a degaussing procedure. Subsequently, we applied a magnetic field of 7.5 mT and recorded the magnetization as the sample was heated from 5 K to 300 K (ZFC). Afterward, we cooled the sample down to 5 K while maintaining the same applied magnetic field, and we recorded the magnetization as the sample was heated from 5 K to 300 K (FC). In addition to this, we also recorded hysteresis loops at 300 K, and these were plotted as a function of the weight of iron oxide present in the capsule.

Magnetic hyperthermia and specific absorption rate (SAR) evaluation. The SAR of each type of IONPs suspended in water or a solid matrix (polyethylene glycol 8000 – PEG 8K) was measured by the calorimetry method. This method involves recording the temperature of the sample for 10 minutes when subjected to an alternating magnetic field (AFM). The device used is an EasyHeat 1.2 kW Induction Heating System from Ambrell. With this system, the amplitude of AFM can be varied from 0 to 65 kA m^{-1} while the AFM frequency was set to 355 kHz. Vials adapted for MH measurements are filled with 0.5 mL of colloidal suspension at an iron concentration of 1 mg mL^{-1}. The heating curves were fitted with the Box–Lucas equation:

$$\Delta T = (S_m/k)(1 - \exp(-k(t - t_0)))$$

where the fitting parameters S_m and k are the initial slope of the heating curve and the constant describing the cooling rate, respectively. The SAR can be calculated as follows:

$$SAR = (c\, m\, S_m)/m_{Fe}$$

where c is the specific heat of the colloid (water is 4186.8 J kg^{-1} K^{-1} and PEG 8k is 2135.27 J kg^{-1} K^{-1}), $m = \rho V$ is the mass of the colloid, taken as the product between the density (water is 0.997 g cm^{-3} and PEG8k is 1.0832 g cm^{-3}) and the volume and m_{Fe} is the mass of iron in the sample. IONPs, dispersed in water at the desired concentrations, were collected at the bottom of the vial using a magnet; the water was removed and hot liquid PEG 8 k (80 °C) was introduced. The dispersion of IONPs on the entire volume of the sample was ensured by immediate sonication with a probe sonicator, followed by sodification without/with the application of a static magnetic field of 65 kA m^{-1} generated using two cubic neodymium magnets with a 3 cm side length.

Photothermia and SAR evaluation. 2 mL of a known concentration of IONP suspension was placed in a 1 cm^3 quartz cuvette (if IONPs suspended in organic solvent) or plastic cuvette (if IONPs suspended in an aqueous medium) and irradiated for 5 min thanks to a near-infrared laser at 1064 nm and a power of 1 W cm^{-2}. A thermal probe was put inside the cuvette to record the temperature during irradiation. After irradiation, the temperature increase as a function of time was plotted and the associated specific absorption rate (SAR) in W g^{-1} was calculated from the experimental curve as described below. As an analogy to the magnetothermal transfer, the

photothermal transfer can be calculated as the specific absorption rate (SAR) in watts per gram of iron oxide absorbing NIR light. This value was calculated by a calorimetric method. By plotting the temperature profiles of the NPs' suspensions subjected to NIR light and then adjusting the experimental curve with a polynomial function, the $[dT/dt]_{t=0, \text{solvent}}$ can be determined. In order to perform precise calculations, the contribution of the solvent in the temperature elevation has to be removed. The calculation of the SAR is thus summed up as

$$\text{SAR} = m_{\text{s}} \frac{C_{\text{S}}}{m_{\text{Fe}_3\text{O}_4}} \times \left(\left[\frac{dT}{dt}\right]_{t=0} - \left[\frac{dT}{dt}\right]_{t=0,\text{solvent}} \right)$$

where m_{s} and C_{S} are, respectively, the mass (in g) and the heat capacity (in J g^{-1} K^{-1}) of the sample, $m_{\text{Fe}_3\text{O}_4}$ (in g) is the mass of iron oxide present in the sample, and $\left[\frac{dT}{dt}\right]_{t=0,\text{solvent}}$ is the derivative function of the solvent. Both of these derivatives are determined the same way as that for MH (*i.e.*, a second order polynomial fit of the temperature curve).

III. Results

III.1. Effect of the FeSt₃ precursor and the reaction temperature range on IONP synthesis

Various synthesis parameters such as the type of precursor, solvent, and ratio were investigated to establish an optimal synthesis protocol for producing 20 nm spherical IONPs.[31,38,39] However, there is still a need to understand how to achieve greater reproducibility in size, composition and defects across multiple synthesis attempts. Two iron stearate precursors, namely FeSt$_2$ and FeSt$_3$, with molar ratios of Fe : St of 1 : 2 and 1 : 3, respectively, were previously examined. It was demonstrated that only FeSt$_3$ allowed obtaining spherical IONPs with a mean size exceeding 15 nm.[31,38] Indeed, FeSt$_2$ is primarily composed of [Fe$_3$-(μ$_3$-O)St$_6$xH$_2$O]Cl, whereas FeSt$_3$ is a mixture composed mainly of [Fe$_7$(μ$_3$-O(H))$_6$(μ$_2$-OH)$_x$St$_{12-2x}$] St, [Fe$_3$(μ$_3$-O)St$_6$·xH$_2$O]St and free stearic acid. FeSt$_3$ exhibits a broader distribution of complexes, with larger Fe complexes exhibiting greater thermal stability, which contribute to the growth step of nuclei.[38] Consequently, the study dedicated to the synthesis of 20 nm spherical IONPs was carried out using homemade FeSt$_3$, synthesized through the coprecipitation of sodium stearate and ferric chloride salts in an aqueous solution, as described in ref. 12, 38 and 39 and the Materials and methods section. Initially, a previously validated protocol for the synthesis of 20 nm sized IONPs with a spinel composition was replicated.[7,31] This protocol (P20_1) involved the use of squalane – which has a boiling point ($T_{\text{B}} = 470$ °C) higher than the targeted temperature[36] – and the addition of a small amount of DBE, aiming to slightly lower the reaction temperature and to provide oxidant species to the reaction media.[7,36,37] Given that only a limited number of IONP syntheses can be performed with one batch of homemade FeSt$_3$, such a study led us to investigate the reproducibility of homemade FeSt$_3$

synthesis in relation to the obtained IONPs. These syntheses were thus conducted with various batches of homemade FeSt$_3$ (denoted as FeSt$_3$-1, FeSt$_3$-2, FeSt$_3$-3, and FeSt$_3$-4) and with a commercial FeSt$_3$ (denoted as FeSt$_3$–TCI).

Multiple batches of synthesized IONPs underwent characterization *via* transmission electron microscopy (TEM) and X-ray diffraction (XRD), with results presented in Table S1.† Despite attempts to maintain a setpoint temperature of 360 °C for reaching a reaction temperature of 330 °C, different reaction temperatures were observed, likely due to the solvent mixture's boiling point.[31] Nevertheless, the TEM mean size of IONPs remained consistent across different temperatures, ranging from 16 to 27 nm, with no correlation between size and temperature. Despite employing the same protocol, variations in mean sizes were evident among batches showing that they were in fact due to variations between homemade FeSt$_3$ batches.

Concerning the IONP composition, the analysis of XRD patterns allows checking the presence of the wüstite phase and consequently of a Fe$_{1-x}$O@Fe$_{3-x}$O$_4$ core–shell structure. The wüstite phase exhibits distinct diffraction peaks at varying Bragg's positions compared to the spinel iron oxide phases, with a different lattice parameter of 4.326 Å (powder diffraction PDF file: 01-089-2468). Thus, this wüstite phase can be identified by XRD. Fig. S2† illustrates a representative XRD pattern of synthesized IONPs using the P20_1 protocol and all diffraction peaks correspond only to the spinel iron oxide phase. Comparison of lattice parameters with bulk magnetite (8.396 Å, PDF file: 00-019-0629) and maghemite (8.351 Å, PDF file: 00-039-1346) indicates that the composition of the NPs is closer to that of magnetite, as expected for NPs with such high mean sizes (Table 1).[11,31,40] The average crystallite sizes deduced from XRD patterns are lower than the TEM sizes which strongly suggests the presence of defects within the IONPs synthesized with the P20_1 protocol.[7,31] Indeed, nuclei in the thermal decomposition process often exhibit a wüstite composition in which oxidation during the growth step leads to defects.[31,32,38] In addition, at the nanoscale, Fe^{2+} ions at the surface of magnetite are easily oxidized leading to a core–shell structure, typical of IONPs with a mean size higher than 12 nm, consisting of a Fe$_{3-x}$O$_4$ core surrounded by an oxidized shell.[11,13]

Significant variations in size were observed among different batches of IONPs. A detailed analysis of homemade precursor structures (detailed in the ESI†) aimed to understand these differences. Characterization studies of homemade and commercial batches (FeSt$_3$–TCI) revealed disparities in carboxylate coordination, polycation type, and thermal stability (Fig. S3†). FeSt$_3$ synthesis is particularly delicate due to the presence of larger iron polycations (MADI-TOFF analysis in Table S1†), making consistent polycation composition control challenging. Consequently, the commercial batch was chosen for further experiments. The thermal decomposition synthesis with this commercial FeSt$_3$ and the P20_1 protocol at 326 °C led to IONPs with a similar spinel composition, a TEM size of 23.0 ± 2.4 nm and a crystallite size of 18.3 nm. Such a discre-

Table 1 Results obtained using the second protocol P20_2 and commercial FeSt₃. $T1$ represents the temperature within the flask during the initial stage for dissolving the reagent and $T2$ represents the final temperature within the flask during the second stage of IONP growth

Synthesis	NP_P20_2_DBE_A	NP_P20_2_DBE_B	NP_P20_2_DBE_C
FeSt₃	FeSt₃–TCI	FeSt₃–TCI	FeSt₃–TCI
$T1$ (°C)	123	123	126
$T2$ (°C)	327	331	336
Mean TEM size (nm)	23.2 ± 2.2	26.1 ± 2.2	26.0 ± 1.7
XRD crystallite size (nm)	17.3 ± 1	18.5 ± 1	26.5 ± 1
Lattice parameter (Å)	8.395 ± 0.001	8.393 ± 0.001	8.393 ± 0.001

pancy between the mean TEM and crystallite sizes was already observed in earlier studies in NPs with similar sizes[7,31] or in nanocubes[33,34] and that was shown to be due to the presence of structural defects by HRTEM. Such HRTEM characterization will be performed below on the most suitable NPs.

With the objective to transfer these IONPs in water and to test them for hyperthermia, attempts were made to coat them with the dendron molecule (Fig. S1†). We thus observed that the reaction temperature required for synthesizing larger IONPs can impact the dendronization step. A ligand exchange was performed in THF to replace OA with dendron molecules. However, applying dendronization to 20 nm IONPs synthesized using a specific protocol resulted in large aggregates in water, indicating unsuccessful dendronization. To understand this, we compared batches from this protocol with those from a standard synthesis method for 10 nm IONPs.[11] The main difference was the reaction temperature: the standard method heated the mixture to the boiling point of octyl ether (290 °C)

for two hours, while the P20_1 protocol heated the reaction mixture to 330 °C for larger IONPs. We hypothesized that prolonged heating at this high temperature may degrade the Fe–OH bonds on the IONPs' surface (left part of Fig. 1), leading to a phenomenon comparable to passivation and resulting in the conversion of Fe–OH bonds to bridging Fe–O–Fe, ultimately affecting the ligand exchange process.

XPS analyses were conducted to verify our hypothesis regarding the surface chemical bonds of two types of IONPs: those produced using the P20-1 protocol (at ≈330 °C) and those synthesized via the 10 nm protocol (at 290 °C). Results indicate a higher intensity of the Fe–OH XPS band (peak at 532 eV) on NPs suitable for dendronization compared to those synthesized at 360 °C for 2 hours (Fig. 1B–D), suggesting a reduced presence of oleic acid molecules and supporting the hypothesis of a bridging Fe–O–Fe bond on their surface. Modifications to the synthesis protocol were necessary to address this dendronization challenge, involving adjustments
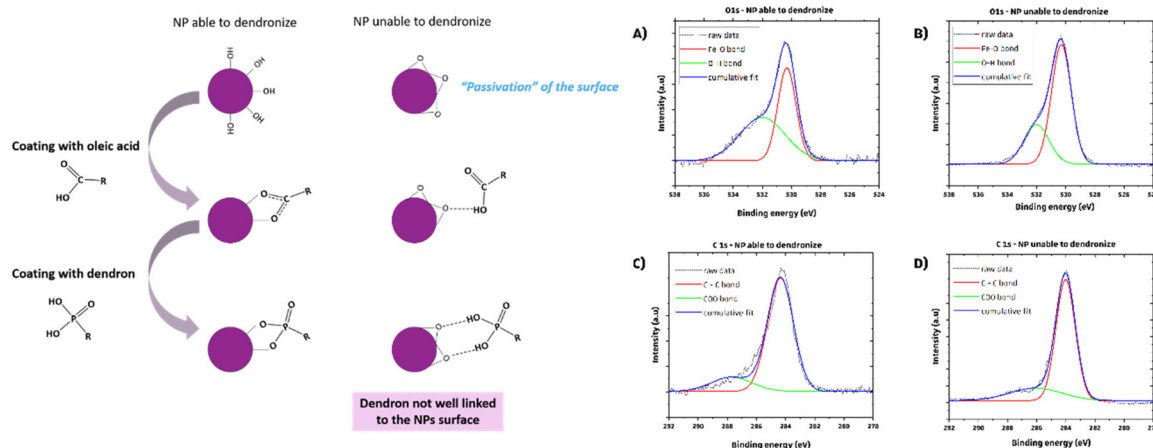

Fig. 1 Left: theoretical scheme depicting the comparison of the dendronization process between two types of NPs: one with the Fe–OH surface group and another NP that was synthesized at an excessively high temperature, resulting in the formation of a Fe–O–Fe bridging bond on its surface. Right: deconvoluted O 1s (A and B) and C 1s (C and D) spectra of two sets of NPs: capable of undergoing successful dendronization (A and C) and unable to do so (B and D).

to heating rate, reaction duration, and temperature. Further studies are needed to optimize the synthesis of 20 nm spherical IONPs for dendronization, including evaluating the role of DBE in the synthesis process.

III.2. Effect of the heating rate and reaction temperature and duration on the size and composition of IONPs

A 2 hour reaction at 330 °C was shown to affect the dendronization step. To address this, two options are proposed: lowering the synthesis temperature to around 310 °C or reducing the reaction time to 330 °C. Lowering the temperature significantly deviates from squalane's boiling point, complicating temperature control and compromising repeatability. It also risks preserving the wüstite core, requiring high temperatures for oxidation and nanoparticle growth. Alternatively, reducing reaction time, though intensifying competition between oxidation and growth kinetics, is more suitable. A new protocol (P20_2) decreases reaction time to one hour and adjusts the $FeSt_3$: OA ratio from 1 : 2 to 1 : 3. OA is recognized for its ability to stabilize the iron precursor, leading to a low yield in nuclei and thus resulting in a high concentration of monomers/precursors available for the growth step[10,39] but also it was expected to allow better control of the reaction temperature. In addition, these specific reactant ratios and amounts have proven successful in previous studies.[1,2,6]

Different batches of monodisperse spherical IONPs, named NP_P20_2_DBE_A, NP_P20_2_DBE_B and NP_P20_2_DBE_C given in Table 1, were thus synthesized. However, the reaction temperature was again difficult to precisely control leading to syntheses with slightly different reaction temperatures and thus different mean IONP sizes: 23 nm at 330 °C and 26 nm at 331 °C and 336 °C.

Syntheses at various temperatures were also performed to assess the impact on reaction outcomes. It was found that the mean diameter of IONPs increased with reaction temperature (Fig. 2A), highlighting the stability and consistency of syntheses using commercial $FeSt_3$. Conversely, inconsistent results were observed when using homemade $FeSt_3$ at different temperatures. This reaffirms the choice of commercial $FeSt_3$ as the iron precursor. Nonetheless, variations in the composition of IONPs were noted depending on the reaction temperature.

When IONPs are synthesized below 325 °C (Table 1), both wüstite and spinel phases are observed in most batches (Fig. S4†), with both phases present in all batches below 322 °C. High-resolution TEM confirmed a core–shell structure (Fig. 2B and C), with surface layers exhibiting different crystallographic structures compared to the core. FFT filtering of HRTEM images identified crystallographic planes for both phases (Fig. 2B and C). These results confirm the formation of a wüstite nucleus under these conditions.[31,32,38] A reaction temperature above 325 °C is necessary for obtaining NPs with a mean size of 23–26 nm and an iron oxide spinel composition. Dendronization is feasible with these IONPs synthesized with a shorter heating duration. Protocol P20_2 is suitable for synthesizing ~20–25 nm IONPs with a monodisperse size distribution and a spinel structure if the reaction temperature is strictly above 325 °C.

III.3. Introduction of defects within IONPs by tuning the synthesis conditions

The impact of dibenzyl ether (DBE) on NP synthesis, particularly regarding NP composition, oxidation process, and defect formation, was further investigated. During the synthesis of IONPs, it has been assessed that the nuclei are constituted of $Fe_{1-x}O$[31,32] and the formation of such $Fe_{1-x}O$ nuclei is again confirmed by these experiments with 0.5 mL of DBE and 19.5 mL of squalene. To achieve spinel iron oxide composition, synthesis conditions need to favor the oxidation kinetics of the
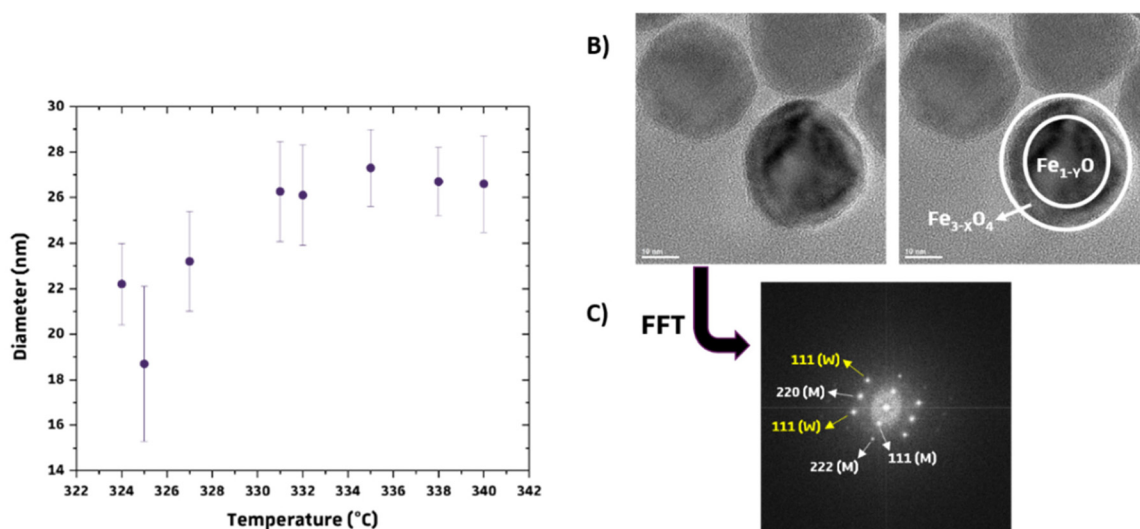

Fig. 2 (A) Mean diameter of IONPs synthesized using protocol P20_2 as a function of the reaction temperature, (B) HRTEM images of core–shell $Fe_{1-x}O@Fe_{3-x}O_4$ IONPs and (C) its corresponding FFT pattern with plane indication (W = wüstite plane, M = magnetite plane) (A).

wüstite phase. Strategies such as adjusting heating rates[31] or employing a "nonaqueous redox phase tuning"[36,37] method involving DBE as an oxidizing agent facilitate defect-free NP synthesis. However, DBE's low boiling point limits NP size. Mixing DBE with hydrocarbon solvents enables the production of nearly defect-free NPs in the 10–30 nm range. Additionally, it was found that dense oleic acid (OA) coatings on NP surfaces inhibit oxidation kinetics, while byproducts from DBE thermolysis[36,37,41] can disrupt these coatings, thereby promoting oxidation kinetics.[31]

To avoid potentially harmful byproducts in biomedical applications, a synthesis method without DBE has been developed consisting in employing a slower heating rate and introducing a nucleation step around 280 °C to favor oxidation kinetics over growth kinetics and/or enhance the oxidation of nuclei before their growth. In addition, as DBE influences the oxidation process limiting the defect formation in resulting IONPs, by omitting DBE, we can produce IONPs with varying defect levels, offering insights into their MH and PTT properties. DBE also influences the shape and composition of IONPs, favoring a uniform spinel structure. We have investigated the impact of DBE quantity, heating rate, and nucleation step on the size, composition, and defects of IONPs.

The influence of varying volumes of DBE on the shape and oxidation kinetics of IONPs was assessed using the P20_2 protocol (Table S2†). Increasing the DBE volume reduced the reaction temperature due to its lower boiling point compared to squalane (298 °C versus 450 °C). Pure DBE hindered the synthesis of significant-sized IONPs, while creating an oxidizing environment. Adding DBE in volumes up to 1 mL resulted in NPs with an average size of 27–32 nm and a spinel composition, promoting size uniformity and oxidation. Further increase in the DBE volume produced more faceted, smaller NPs, resembling cubic shapes, consistent with previous studies.[8,37] The lower reaction temperature and by-products from DBE thermolysis contributed to smaller NPs and a maghemite-like composition. Mixing equal volumes of squalane and DBE yielded well-defined, homogeneous NPs but was deemed less ideal due to safety concerns with the mixture's instability at high temperatures. The ratio of crystallite size to TEM size indicated a positive impact of DBE, although some synthesis conditions introduced an oxidized layer with defects.

To maintain size homogeneity and enhance oxidation kinetics during the synthesis of IONPs with a spinel composition akin to magnetite, incorporating a minimal amount of DBE (0.5 to 1 mL) is necessary due to its crucial role in the oxidation process. Magnetite composition is preferred for its higher M_s and protection against further oxidation is provided by the dendronization thanks to the presence of the two anchoring phosphonate groups.[33,42] Efforts have been then made to adjust the protocol to improve oxidation kinetics without relying on DBE while ensuring size uniformity.

The syntheses have been thus conducted by implementing a slower heating rate and incorporating a nucleation step in order to establish a bett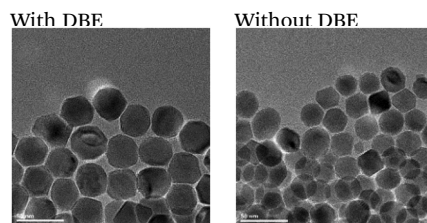er equilibrium between the growth and oxidation kinetics without relying on an oxidizing component like DBE. The nucleation step was set at 280 °C for 30 min, based on FeSt$_3$ TGA/DTA curves (Fig. 2) and prior studies.[31,32,39,43,44] The heating rate was reduced to 1 °C min^{-1}, down from 5 °C min^{-1}, until the 60 minute growth stage at 330 °C. This revised method, labeled P20_3, was evaluated with and without DBE, with results summarized in Table 2. It enables the synthesis of spherical IONPs with a spinel composition and significant average size, eliminating the need for DBE. However, particle size uniformity is slightly reduced compared to the P20_2 protocol, with sizes exceeding 20 nm, adjustable via the reaction temperature.

The composition's homogeneity is crucial, being evident from comparable XRD patterns of both batches (Fig. S5†), showing similar characteristics, predominantly iron oxide spinel peaks with lattice parameters akin to magnetite. However, a faint XRD peak in NP_P20_3_no_DBE suggests a minor presence of the wüstite phase. Introduction of DBE leads to larger IONPs (>30 nm), possibly altering nucleation and growth. Reproducibility studies reported in Table S3† confirm promising results with lower reaction temperature, albeit slightly more heterogeneous size distribution compared to the previous protocol (P20_2). Additionally, the ratio of crystallite size to TEM size indicates the presence of defects in these IONPs.

The P20_3_no_DBE protocol allowed for the synthesis of uniform 20–25 nm IONPs without using DBE. However, careful temperature control is still essential to maintain composition uniformity, as low temperatures can hinder wüstite core oxidation. Our study confirms the feasibility of synthesizing these nanoparticles with or without DBE. When DBE is omitted, there is a slight reduction in size uniformity, which is not expected to significantly affect magnetic properties. Nonetheless, its absence may affect oxidation kinetics, potentially altering nanoparticle defect levels.

Table 2 Results obtained with the protocol P20_3 with and without DBE. $T1$ represents the temperature with the flask during the first step to dissolve the reagent, $T_{nucleation}$ represents the temperature within the flask during the nucleation step, and $T2$ represents the final temperature within the flask during the second step of IONP growth

Synthesis	With DBE	Without DBE
FeSt$_3$	FeSt$_3$–TCI	FeSt$_3$–TCI
$T1$ (°C)	121	121
$T_{nucleation}$ (°C)	285	282
$T2$ (°C)	329	326
Mean TEM size (nm)	33.3 ± 3.2	25.4 ± 3.0
XRD crystallite size (nm)	26.2 ± 1	23.3 ± 1
Lattice parameter (Å)	8.391 ± 0.001	8.393 ± 0.001
Ratio of crystallite size to TEM size	0.79	0.929

Oxidized core–shell IONPs. Two protocols were established to produce 20–25 nm spherical IONPs with consistent spinel composition but varying levels of defects. Despite this, various synthesis methods can yield core–shell spherical IONPs with a wüstite core and magnetite shell. Exploring the potential of subjecting these batches to thermal treatment to oxidize the wüstite phase into magnetite and potentially modify defect levels, 22 nm spherical IONPs (NP_CS) with a $Fe_{1-Y}O@Fe_{3-X}O_4$ core–shell structure were oxidized, resulting in NP_CS_ox. In brief, 5 mL of IONP suspension in THF was mixed with 5 mL of oleic acid (OA) and stirred for 30 minutes at 120 °C. The TEM size, lattice parameters, and crystallite size of NP_CS and NP_CS_ox were compared *via* XRD refinement (Table 3), alongside results from established protocols P20_2 and P20_4_no_DBE. XRD diffractograms (Fig. S6†) and refinement data (Table 3) show disappearance of the wüstite phase following post-oxidation, suggesting the potential of core–shell synthesis with thermal treatment.

III.4. Evaluation of the amount of defects in IONPs

The demand to quantify defects in IONPs has grown due to their impact on MH and PTT treatments. Various methods exist for characterizing IONPs to evaluate defects. X-ray pattern refinement determines the crystallite size, reflecting the size of the diffracting domain. A NP's crystallite size typically matches its TEM size if it is monocrystalline. However, structural defects can create smaller crystalline domains. A NP with few defects shows a close match between crystallite and TEM sizes, while numerous defects result in a smaller crystallite size. Comparing these sizes allows for an initial assessment of defects, but other techniques should be used for accuracy, considering variations in measurement methods. Table 4 compares this ratio for batches from different synthesis methods, providing initial insights into potential structural defects.

Comparing crystallite sizes to determine defect amounts is challenging due to sample variability in size from the P20_3_no_DBE protocol. Among eight samples from two synthesis protocols, NPs from the P20_2 protocol (with DBE) show

Table 3 Comparison of mean TEM size, crystallite size and lattice parameters of a core–shell IONP batch ($Fe_{1-Y}O@Fe_{3-X}O_4$) before and after oxidation treatment

	NP_CS	NP_CS_ox
Synthesis	FeSt$_3$	
	FeSt$_3$–TCI	FeSt$_3$–TCI
Mean TEM size (nm)	22.6 ± 2.3	23.2 ± 1.7
XRD crystallite size (nm)	—	18.3 ± 1
Lattice parameter (Å)	—	8.393 ± 0.001
Ratio of crystallite size to TEM size	—	0.79

Table 4 Comparison between mean crystallite size and TEM size from various batches synthesized with P20_2 and P20_3_no_DBE protocols
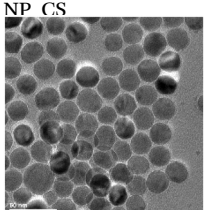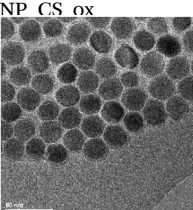
	TEM size (±2 nm)	Crystallite size (±1 nm)	Ratio	Mean ratio
NP_P20_2 (with DBE)	26.6	25.2	0.95	0.96 ± 0.06
	22.2	19.3	0.87	
	26.7	26.5	0.99	
	26.0	26.5	1.01	
NP_P20_3_no_DBE (without DBE)	23.9	23.4	0.98	0.85 ± 0.09
	22.9	19.2	0.84	
	23.7	17.8	0.75	
	18.0	15.2	0.84	
NP_P20_CS_ox	23.2	18.3	0.79	—

closely aligned average crystallite sizes with TEM measurements. Additionally, their crystallite size ratio consistently indicates fewer defects, confirming DBE's role in creating an oxidizing environment during synthesis, favorable for fewer defects in IONPs. The oxidation treatment of core–shell IONPs yields a slightly lower ratio than that of P20_3_no_DBE batches, suggesting that the oxidation promoted defects as expected.

The HRTEM images show crystallographic planes in the studied IONPs, with FFT revealing irregularities like stacking faults or dislocations (Fig. 3).[7,33] In Fig. 3, inverse FFT results from magnetite lattice planes (111) and (222) in IONPs synthesized with P20_2 and P20_3_no_DBE protocols are compared. Notably, the P20_3_no_DBE protocol showed a higher prevalence of defects, particularly edge dislocations, compared to P20_2. While the analysis is not quantitative, it strongly suggests that IONPs from the P20_3_no_DBE protocol have qualitatively more defects than those from the P20_2 protocol.

A comparative analysis was conducted to determine the band gap and Urbach energy (Fig. S7† and Table 5) of various batches of IONPs from their UV-vis spectra (Fig. S8†). Urbach energy (E_u) levels are closely related to the presence of defects,[45,46] particularly in semiconductor oxides like magnetite, where localized defect states,[30,47] such as oxygen vacancies, can reduce the band gap. Higher E_u values (Fig. S7–S9†) indicate more defects, suggesting an imperfect conduction band.[26,45,47,48] The band gap energy remains consistent across samples (3.5 ± 0.2 eV), but significant differences in E_u are observed between batches synthesized with and without DBE. Samples synthesized with DBE show lower E_u values, indicating fewer defects from oxygen vacancies. Attempts to replicate the effects of DBE by altering synthesis parameters (P20_3_no_DBE protocol) result in spinel structure NPs with both point and structural defects. Urbach energy increases notably in samples synthesized after an oxidation treatment, likely due to more oxidation sites from the wüstite core oxidation process.

III.5. Magnetic properties and heating capabilities of IONP suspensions

The impact of the wüstite core, spinel composition, and defect amount on magnetic properties and heating abilities of 20–25 nm spherical IONPs was investigated. This included
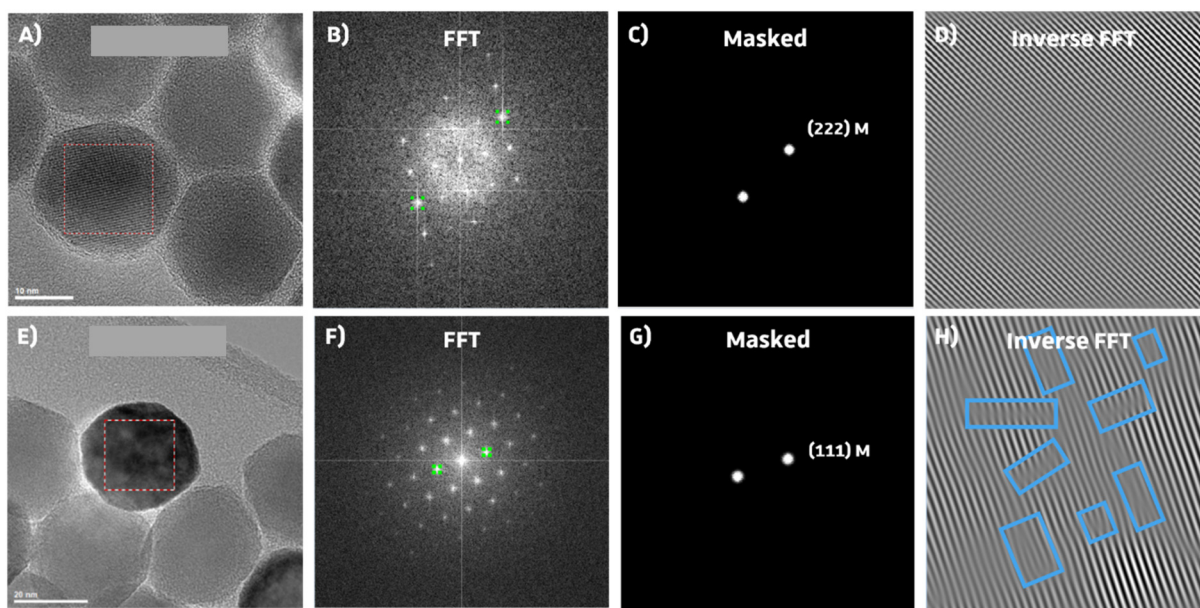
Fig. 3 Upper row corresponds to IONPs synthesized with protocol P20_2 and the lower row corresponds to IONPs synthesized with protocol P20_3_no_DBE. (A) and (E) High resolution TEM images of IONPs, (B) and (F) the corresponding FFT images, (C) and (G) applied masked on two reflections plans, and (D) and (H) inverse FFT to visualize the crystallographic planes and eventual defects. Blue squares show crystallographic defects.

Table 5 Calculated E_g and E_u from various batches synthesized with P20_2 and P20_3_no_DBE protocols

Protocol	Batch	E_g ($\pm$0.2 eV)	E_u (eV)
P20_2 (with DBE)	NP_P20_DBE_1	3.4	0.6
	NP_P20_DBE_2	3.5	0.7
	NP_P20_DBE_3	3.7	0.7
P20_3_no_DBE (without DBE)	NP_P20_NO_DBE_1	3.5	1.2
	NP_P20_NO_DBE_2	3.4	1.2
	NP_P20_NO_DBE_3	3.4	0.9
Oxidation process	NP_CS_ox	3.4	1.4

IONPs from protocols P20_2 and P20_3_no_BDE (NP_20_DBE and NP_20_no_BDE), core–shell IONPs (NP_20_CS), and their oxidized counterparts (NP_20_CS_ox). Magnetic properties were initially measured using SQUID (Fig. 4). Heating capabilities were then studied *via* MH after dendronization of IONPs, whose colloidal stability was assessed by DLS measurements (Fig. S10†).

All samples show quite a superparamagnetic behavior at 300 K (Fig. 4A) with a very small hysteresis with a coercive field lower than 0.01T. NP_20_DBE and NP_20_no_DBE exhibit high M_s values of 88 emu g^{-1} and 83 emu g^{-1}, respectively, close to bulk magnetite (94 emu g^{-1}). The core–shell sample also demonstrates a high M_s of 64 emu g^{-1}, increasing to 74 emu g^{-1} upon post-oxidation treatment. ZFC and FC curves (Fig. S4B†) reveal high blocking temperatures typical of IONPs of this size range (20–50 nm) due to significant dipolar interactions.[49] For the NP_20_DBE sample, there is a noticeable

increase in magnetization around 90 K in both the ZFC and FC curves. This increase is attributed to the Verwey transition, which is a characteristic feature of magnetite. The shift of the Verwey transition temperature below 110 K (the usual value for MNPs) has been linked to non-stoichiometric magnetite caused by the presence of Fe^{2+} vacancies.[50] The onset of the Verwey transition is nearly undetectable in the NP_20_no_DBE sample. In contrast, it is quite evident in the core–shell sample. Additionally, the core–shell sample shows a significant increase in magnetization between 225 and 275 K. This feature cannot be related to the Néel transition of wüstite, which is expected around 200 K, but is instead attributed to a highly "disordered" magnetic phase referred to as the X-phase by other groups.[51,52] In the oxidized sample, the Verwey transition becomes more prominent than the X-phase transition, indicating the dominance of the magnetite phase, as reflected in the increased M_s.

In the initial stage of the MH study, the heat generation capabilities of four types of iron oxide nanoparticles (IONPs) suspended in water (1 mg$_{Fe}$ mL^{-1}) were examined. Specific absorption rate (SAR) values were plotted against the amplitude (H) of alternating magnetic field (AMF), ranging from 5 kA m^{-1} to 60 kA m^{-1}, at a fixed frequency of 355 kHz. To ensure accuracy, the contribution from pure water at each H was subtracted. IONPs from the NP_20_CS batch, with a core–shell architecture, showed moderate SAR values, increasing slightly with H from 75 W g$_{Fe}^{-1}$ at 5 kA m^{-1} to 475 W g$_{Fe}^{-1}$ at 60 kA m^{-1}. In contrast, NP_20_CS_ox exhibited a significant enhancement in heating performance, with SAR values nearly doubling at each H value, ranging from 130 W g$_{Fe}^{-1}$ to 850 W
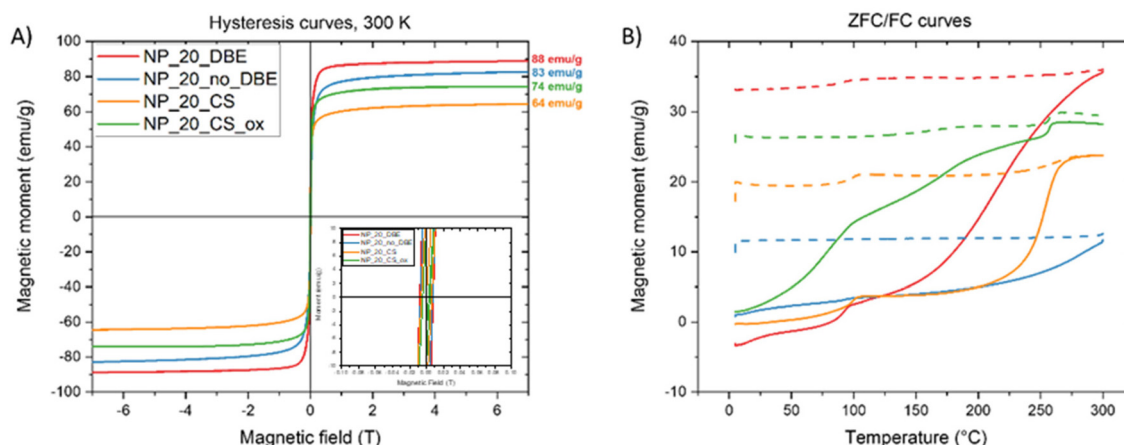
Fig. 4 (A) Magnetization curves (insert: zoom between −0.1 and 0.1 T) and (B) ZFC/FC curve of four types of IONPs.

g_{Fe}^{-1} as H increased. This improvement is attributed to the conversion of the magnetically inactive würstite core into magnetite/maghemite. IONPs produced using the P20_3_no_BDE protocol, containing defects within their structure and exhibiting a high M_s value, showed higher SAR values over the entire H range compared to previous IONPs, ranging from 80 W g_{Fe}^{-1} to 1525 W g_{Fe}^{-1}. The presence of defects within the spinel structure contributed to this increase. IONPs from the NP_20_DBE batch, with reduced defects in their spinel structure and the highest M_s value, yielded the highest SAR values, reaching 1680 W g_{Fe}^{-1} at 30 kA m^{-1} and 2150 W g_{Fe}^{-1} at 60 kA m^{-1}. These IONPs demonstrate significantly enhanced heating capabilities, surpassing established or revised safety limits for magnetic hyperthermia treatment, with SAR values of 780 W g_{Fe}^{-1} at 15 kA m^{-1} and 1470 W g_{Fe}^{-1} at 25 kA m^{-1}.

Based on the above analysis, IONPs produced using both P20_2 and P20_3_no_DBE protocols are promising for further *in vitro* and *in vivo* MH studies. However, within cells, IONPs are confined to lysosomes, limiting their Brownian motion and relying solely on Néel relaxation for heating. To investigate this, IONPs were immobilized in a PEG8k matrix, either ran-

domly or prealigned under a static magnetic field (strength of 65 kA m^{-1}). SAR values significantly decrease when IONPs are immobilized in PEG, reducing Brownian motion by 68% for NP_P20_DBE and 78% for NP_P20_3_no_DBE (Fig. 5B and C). When the IONPs are prealigned within the solid matrix with their easy axis of magnetization being parallel to AMF lines, the Néel contribution is increased, restoring SAR values by up to 50% compared to water (Fig. 5B and C). However, one may notice that even if the SAR values of IONPs with DBE decrease when they are immobilized, they stay always higher than those of IONPs without DBE. Therefore, IONPs with DBE are the most performant for MH.

For photothermal experiments, suspensions of IONPs at 0.05 mg_{Fe} mL^{-1} in chloroform were exposed to a 1064 nm laser at 1 W cm^{-2} for 3 minutes. A chloroform-only sample served as a control. Temperature was monitored continuously, and temperature changes over time were plotted. IONPs consistently led to significant temperature increases compared to the control. However, discerning a clear trend between synthesis protocols P20_2 and P20_3_no_DBE was challenging, as their temperature–time curves showed similar patterns.
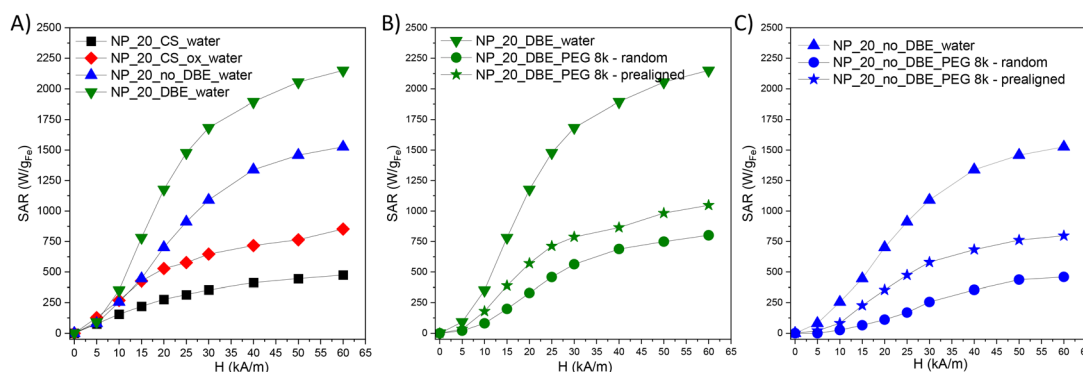

Fig. 5 (A) SAR values for NP_P20_DBE, NP_P20_no_DBE, NP_20_CS and NP_20_CS_ox suspensions in water and of (B) NP_20_DBE and (C) NP_20_no_DBE suspended in water and in a PEG8k matrix, random or prealigned, at a concentration of 1 mg_{Fe} mL^{-1}.

Table 6 SAR values by photothermia of IONPs synthesized with the P20_2 and P20_3_no_DBE protocols (1064 nm, 1 W cm^{-2}) at a concentration of 0.05 mg$_{Fe}$ mL^{-1}

Protocol	Batch	SAR (W g^{-1})	E_u (±0.2 eV)
P20_2	NP_P20_2_DBE_2	548	0.6
	NP_P20_2_DBE_3	540	0.7
P20_3_no_DBE	NP_P20_3_no_DBE_1	412	1.2
	NP_P20_3_no_DBE_3	497	0.9

Nonetheless, batches synthesized with DBE (P20_2) generally exhibited slightly higher temperature increases compared to those without DBE (P20_3_no_DBE).

Comparing SAR values (Table 6), batches synthesized with the P20_2 protocol show slightly higher values than those with P20-3_no_DBE and a correlation of SAR values with the Urbach energy is observed.[30] The SAR values decrease when the Urbach energy increases, but for an Urbach energy of 0.6, the SAR value is 548 W g^{-1} when it is 412 W g^{-1} when the energy is two times higher. Further measurements on a broader range of Urbach energy are recommended to confirm this correlation between vacancy defect levels and PTT efficiency. However, IONPs with DBE exhibit notable heating properties even at low concentrations (0.05 mg$_{Fe}$ mL^{-1}).

MH measurements indicated that SAR values of IONPs in suspension increase with M_s values, primarily due to Brownian relaxation. Experiments with immobilized IONPs confirmed that defects favor Néel relaxation.[7,23] However, IONPs synthesized with DBE with less defects, showed higher SAR values even when immobilized in a matrix and they are thus preferable for both *in vitro* and *in vivo* MH applications. Regarding PTT measurements, an impact of defects and especially a correlation with Urbach energy is noted suggesting thus an impact of defects.[30] Consequently, the protocol utilizing DBE in our experimental conditions and leading to fewer defects appears optimal for achieving IONPs with superior performance in both MH and PTT.

IV. Conclusion

The objectives were to synthesize IONPs with a mean size of 20–25 nm and a spinel composition exhibiting different "amounts" of defects as defects were more and more demonstrated to impact MH and PTT performances. The synthesis of IONPs with a mean size higher than 20 nm and a spinel composition by the thermal method is always challenging as nuclei with a wüstite composition are formed and thus there is a big issue in controlling both the grain growth and the oxidation kinetics after the nucleation step. The most used approach to face this problem is the addition of DBE, an oxidizing agent, in the reaction media, which avoids obtaining a core–shell structure with a wüstite core and a spinel iron oxide shell and leads to defect free iron oxide spinel NPs. However, DBE can introduce harmful by-products. Therefore, we have

tuned different synthesis parameters using the thermal decomposition method to try to avoid the use of DBE and the most important objective here was to synthesize IONPs with a spinel composition and different defect densities.

A commercial iron stearate precursor was chosen for reproducibility over homemade ones due to the difficulty in controlling the complex polycation distributions in homemade precursors. Various protocols were tested, revealing optimal conditions of a 1 hour reaction duration and 330 °C reaction temperature to avoid core–shell structure formation. The significance of DBE as an oxidizing agent in producing defect-free IONPs was emphasized by varying its quantity. It was observed that using approximately 0.5 or 1 mL of DBE was adequate to produce IONPs sized around 20–25 nm with a spinel composition. Higher amounts of DBE led to IONPs with cubic shapes and a maghemite composition. Additionally, experiments involving a slower heating rate and a nucleation step, with or without DBE, showed that this protocol could yield IONPs with a spinel composition even in the absence of DBE. Consequently, two distinct protocols have been established for synthesizing IONPs with an average size between 20 and 25 nm, with or without DBE.

The magnetic measurements indicated that IONPs synthesized with DBE had higher M_s values compared to those synthesized without DBE, suggesting a composition similar to that of magnetite. Structural defects were examined using XRD and HRTEM, while point defects like vacancies were assessed by calculating Urbach energy from UV spectra. IONPs synthesized without DBE exhibited more structural defects and higher Urbach energies, indicating the presence of more point defects, in contrast to those synthesized with DBE.

MH and PTT experiments were conducted to evaluate how defects in the spinel structure affect hyperthermia performance. Both experiments indicated that IONPs without defects would show enhanced PTT and MH SAR values. Specifically, IONPs synthesized with DBE showed higher SAR values due to reduced defect content and higher M_s, but SAR values halved when immobilized in a solid matrix. IONPs synthesized without DBE, with more defects, had lower SAR values, but the decrease was less pronounced when immobilized in the solid matrix, indicating less influence of Brownian relaxation. However, even if the SAR values of IONPs with DBE decrease when they are immobilized in a matrix, the SAR values stay higher than those of IONPs synthesized without DBE. PTT measurements showed slightly larger SAR values for IONPs with DBE compared to those without and a correlation is noticed. Other results on a broader range of Urbach energy would be necessary to unambiguously conclude about this correlation. Therefore, IONPs synthesized with DBE exhibiting fewer defects are the best performing ones to combine both MH and PTT in one formulation.

Data availability

The data supporting this article have been included as part of the ESI.†

Conflicts of interest

There is no conflict of interest to declare.

Acknowledgements

References

1 G. Cotin, C. B. Andujar, D. V. Nguyen, C. Affolter-Zbaraszczuk, S. Boutry, A. Boos, P. Ronot, B. Uring, P. Choquet, P. E. Zorn, D. Mertz, S. Laurent, R. N. Muller, F. Meyer, D. Felder-Flesch and S. Begin, *Nanotechnology*, 2019, **30**, 374002.

2 C. Blanco-Andujar, A. Walter, G. Cotin, C. Bordeianu, D. Mertz, D. Felder-Flesch and S. Begin-Colin, *Nanomedicine*, 2016, **11**, 1889–1910.

3 A. E. Deatsch and B. A. Evans, *J. Magn. Magn. Mater.*, 2014, **354**, 163–172.

4 A. Espinosa, R. Di Corato, J. Kolosnjaj-Tabi, P. Flaud, T. Pellegrino and C. Wilhelm, *ACS Nano*, 2016, **10**, 2436–2446.

5 S. Cabana, A. Curcio, A. Michel, C. Wilhelm and A. Abou-Hassan, *Nanomaterials*, 2020, **10**, 1548.

6 B. Freis, G. Cotin, F. Perton, D. Mertz, S. Boutry, S. Laurent and S. Begin-Colin, in *Magnetic Nanoparticles in Human Health and Medicine*, 2021, pp. 380–429.

7 G. Cotin, C. Blanco-Andujar, F. Perton, L. Asín, J. M. de la Fuente, W. Reichardt, D. Schaffner, D.-V. Ngyen, D. Mertz, C. Kiefer, F. Meyer, S. Spassov, O. Ersen, M. Chatzidakis, G. A. Botton, C. Hénoumont, S. Laurent, J.-M. Greneche, F. J. Teran, D. Ortega, D. Felder-Flesch and S. Begin-Colin, *Nanoscale*, 2021, **13**, 14552–14571.

8 P. Guardia, R. Di Corato, L. Lartigue, C. Wilhelm, A. Espinosa, M. Garcia-Hernandez, F. Gazeau, L. Manna and T. Pellegrino, *ACS Nano*, 2012, **6**, 3080–3091.

9 R. D. Corato, A. Espinosa, L. Lartigue, M. Tharaud, S. Chat, T. Pellegrino, C. Ménager, F. Gazeau and C. Wilhelm, *Biomaterials*, 2014, **35**, 6400–6411.

10 A. Hervault and N. T. K. Thanh, *Nanoscale*, 2014, **6**, 11553–11573.

11 W. Baaziz, B. P. Pichon, S. Fleutot, Y. Liu, C. Lefevre, J.-M. Greneche, M. Toumi, T. Mhiri and S. Begin-Colin, *J. Phys. Chem. C*, 2014, **118**, 3795–3810.

12 G. Cotin, C. Kiefer, F. Perton, D. Ihiawakrim, C. Blanco-Andujar, S. Moldovan, C. Lefevre, O. Ersen, B. Pichon, D. Mertz and S. Bégin-Colin, *Nanomaterials*, 2018, **8**, 881.

13 J. Santoyo Salazar, L. Perez, O. de Abril, L. Truong Phuoc, D. Ihiawakrim, M. Vazquez, J.-M. Greneche, S. Begin-Colin and G. Pourroy, *Chem. Mater.*, 2011, **23**, 1379–1386.

14 A. Sathya, P. Guardia, R. Brescia, N. Silvestri, G. Pugliese, S. Nitti, L. Manna and T. Pellegrino, *Chem. Mater.*, 2016, **28**, 1769–1780.

15 M. Levy, A. Quarta, A. Espinosa, A. Figuerola, C. Wilhelm, M. García-Hernández, A. Genovese, A. Falqui, D. Alloyeau, R. Buonsanti, P. D. Cozzoli, M. A. García, F. Gazeau and T. Pellegrino, *Chem. Mater.*, 2011, **23**, 4170–4180.

16 F. Gazeau, M. Lévy and C. Wilhelm, *Nanomedicine*, 2008, **3**, 831–844.

17 J. Mohapatra, A. Mitra, D. Bahadur and M. Aslam, *CrystEngComm*, 2013, **15**, 524–532.

18 J. G. Ovejero, D. Cabrera, J. Carrey, T. Valdivielso, G. Salas and F. J. Teran, *Phys. Chem. Chem. Phys.*, 2016, **18**, 10954–10963.

19 D. Cabrera, A. Coene, J. Leliaert, E. J. Artes, N. D. Telling and F. J. Teran, *ACS Nano*, 2018, **12**, 2741–2752.

20 C. Iacovita, G. F. Stiufiuc, R. Dudric, N. Vedeanu, R. Tetean, R. I. Stiufiuc and C. M. Lucaciu, *Magnetochemistry*, 2020, **6**, 23.

21 C. Iacovita, R. Stiufiuc, T. Radu, A. Florea, G. Stiufiuc, A. Dutu, S. Mican, R. Tetean and C. M. Lucaciu, *Nanoscale Res. Lett.*, 2015, **10**, 391.

22 D. Soukup, S. Moise, E. Céspedes, J. Dobson and N. D. Telling, *ACS Nano*, 2015, **9**, 231–240.

23 A. Lak, M. Cassani, B. T. Mai, N. Winckelmans, D. Cabrera, E. Sadrollahi, S. Marras, H. Remmer, S. Fiorito, L. Cremades-Jimeno, F. J. Litterst, F. Ludwig, L. Manna, F. J. Teran, S. Bals and T. Pellegrino, *Nano Lett.*, 2018, **18**, 6856–6866.

24 A. Lappas, G. Antonaropoulos, K. Brintakis, M. Vasilakaki, K. N. Trohidou, V. Iannotti, G. Ausanio, A. Kostopoulou, M. Abeykoon, I. K. Robinson and E. S. Bozin, *Phys. Rev. X*, 2019, **9**, 041044.

25 A. Lak, S. Disch and P. Bender, *Adv. Sci.*, 2021, **8**, 2002682.

26 M. E. Sadat, M. Kaveh Baghbador, A. W. Dunn, H. P. Wagner, R. C. Ewing, J. Zhang, H. Xu, G. M. Pauletti, D. B. Mast and D. Shi, *Appl. Phys. Lett.*, 2014, **105**, 091903.

27 T.-J. Yu, P.-H. Li, T.-W. Tseng and Y.-C. Chen, *Nanomedicine*, 2011, **6**, 1353–1363.

28 A. Espinosa, J. Kolosnjaj-Tabi, A. Abou-Hassan, A. Plan Sangnier, A. Curcio, A. K. A. Silva, R. Di Corato, S. Neveu, T. Pellegrino, L. M. Liz-Marzán and C. Wilhelm, *Adv. Funct. Mater.*, 2018, **28**, 1803660.

29 C. Lozano-Pedraza, E. Plaza-Mayoral, A. Espinosa, B. Sot, A. Serrano, G. Salas, C. Blanco-Andujar, G. Cotin, D. Felder-

Flesch, S. Begin-Colin and F. J. Teran, *Nanoscale Adv.*, 2021, **3**, 6490–6502.

30 E. Bertuit, E. Benassai, G. Mériguet, J.-M. Greneche, B. Baptiste, S. Neveu, C. Wilhelm and A. Abou-Hassan, *ACS Nano*, 2022, **16**, 271–284.

31 G. Cotin, F. Perton, C. Petit, S. Sall, C. Kiefer, V. Begin, B. Pichon, C. Lefevre, D. Mertz, J.-M. Greneche and S. Begin-Colin, *Chem. Mater.*, 2020, **32**, 9245–9259.

32 G. Cotin, B. Heinrich, F. Perton, C. Kiefer, G. Francius, D. Mertz, B. Freis, B. Pichon, J. Strub, S. Cianférani, N. Ortiz Peña, D. Ihiawakrim, D. Portehault, O. Ersen, A. Khammari, M. Picher, F. Banhart, C. Sanchez and S. Begin-Colin, *Small*, 2022, 2200414.

33 A. Walter, C. Billotey, A. Garofalo, C. Ulhaq-Bouillet, C. Lefèvre, J. Taleb, S. Laurent, L. Vander Elst, R. N. Muller, L. Lartigue, F. Gazeau, D. Felder-Flesch and S. Begin-Colin, *Chem. Mater.*, 2014, **26**, 5252–5264.

34 B. P. Pichon, O. Gerber, C. Lefevre, I. Florea, S. Fleutot, W. Baaziz, M. Pauly, M. Ohlmann, C. Ulhaq, O. Ersen, V. Pierron-Bohnes, P. Panissod, M. Drillon and S. Begin-Colin, *Chem. Mater.*, 2011, **23**, 2886–2900.

35 E. Wetterskog, C.-W. Tai, J. Grins, L. Bergström and G. Salazar-Alvarez, *ACS Nano*, 2013, **7**, 7132–7144.

36 R. Chen, M. G. Christiansen, A. Sourakov, A. Mohr, Y. Matsumoto, S. Okada, A. Jasanoff and P. Anikeeva, *Nano Lett.*, 2016, **16**, 1345–1351.

37 P. Guardia, A. Riedinger, S. Nitti, G. Pugliese, S. Marras, A. Genovese, M. E. Materia, C. Lefevre, L. Manna and T. Pellegrino, *J. Mater. Chem. B*, 2014, **2**, 4426.

38 F. Perton, G. Cotin, C. Kiefer, J.-M. Strub, S. Cianferani, J.-M. Greneche, N. Parizel, B. Heinrich, B. Pichon, D. Mertz and S. Begin-Colin, *Inorg. Chem.*, 2021, **60**, 12445–12456.

39 G. Cotin, C. Kiefer, F. Perton, M. Boero, B. Özdamar, A. Bouzid, G. Ori, C. Massobrio, D. Begin, B. Pichon, D. Mertz and S. Begin-Colin, *ACS Appl. Nano Mater.*, 2018, **1**, 4306–4316.

40 A. Demortière, P. Panissod, B. P. Pichon, G. Pourroy, D. Guillon, B. Donnio and S. Bégin-Colin, *Nanoscale*, 2011, **3**, 225–232.

41 K. E. Gilbert and J. J. Gajewski, *J. Org. Chem.*, 1982, **47**, 4899–4902.

42 T. J. Daou, J. M. Grenèche, G. Pourroy, S. Buathong, A. Derory, C. Ulhaq-Bouillet, B. Donnio, D. Guillon and S. Begin-Colin, *Chem. Mater.*, 2008, **20**, 5869–5875.

43 S. G. Kwon, Y. Piao, J. Park, S. Angappane, Y. Jo, N.-M. Hwang, J.-G. Park and T. Hyeon, *J. Am. Chem. Soc.*, 2007, **129**, 12571–12584.

44 L. M. Bronstein, X. Huang, J. Retrum, A. Schmucker, M. Pink, B. D. Stein and B. Dragnea, *Chem. Mater.*, 2007, **19**, 3624–3632.

45 B. Choudhury and A. Choudhury, *Phys. E*, 2014, **56**, 364–371.

46 H. El Ghandoor, H. M. Zidan, M. M. H. Khalil and M. I. M. Ismail, *Int. J. Electrochem. Sci.*, 2012, **7**, 5734–5745.

47 V. R. Akshay, B. Arun, G. Mandal and M. Vasundhara, *Phys. Chem. Chem. Phys.*, 2019, **21**, 12991–13004.

48 S. M. Wasim, C. Rincón, G. Marín, P. Bocaranda, E. Hernández, I. Bonalde and E. Medina, *Phys. Rev. B: Condens. Matter Mater. Phys.*, 2001, **64**, 195101.

49 M. A. Gonzalez-Fernandez, T. E. Torres, M. Andrés-Vergés, R. Costo, P. de la Presa, C. J. Serna, M. P. Morales, C. Marquina, M. R. Ibarra and G. F. Goya, *J. Solid State Chem.*, 2009, **182**, 2779–2784.

50 A. R. Muxworthy and E. McClelland, *Geophys. J. Int.*, 2000, **140**, 101–114.

51 I. Castellanos-Rubio, I. Rodrigo, R. Munshi, O. Arriortua, J. S. Garitaonandia, A. Martinez-Amesti, F. Plazaola, I. Orue, A. Pralle and M. Insausti, *Nanoscale*, 2019, **11**, 16635–16649.

52 C. P. Guntlin, S. T. Ochsenbein, M. Wörle, R. Erni, K. V. Kravchyk and M. V. Kovalenko, *Chem. Mater.*, 2018, **30**, 1249–1256.